chemosensors

MDPI

Review

Fluorogenic Probe-Coupled Single-Molecule Fluorescence Imaging for Photocatalytic Mechanism Research

Zeqi Yu [1,2,†], Xinyu Sun [1,2,†], Yanan Niu [2,3], Chaoyu Song [1,2,4,*], Yukang Sun [5,*] and Yuguang Lv [1,2]

1 School of Pharmacy, Jiamusi University, Jiamusi 154007, China; 13836726770@163.com (Z.Y.); 15774676244@163.com (X.S.); yuguanglv@163.com (Y.L.)
2 College of Materials Science and Engineering, Jiamusi University, Jiamusi 154007, China; m18310045776@163.com
3 School of Art and Design, Qiqihar University, Qiqihar 161006, China
4 College of Chemistry and Chemical Engineering, Shanghai Jiaotong University, Shanghai 200240, China
5 State Key Laboratory of Green Building Materials, China State Building Materials, Research Institute, Chaoyang District, Beijing 100024, China
* Correspondence: songchaoyu@sjtu.edu.cn (C.S.); yukangsun@ctc.ac.cn (Y.S.)
† These authors contributed equally to this work.

Abstract

Elucidating structure–activity relationships in semiconductor photocatalysis has been significantly impeded by the inherent limitations of ensemble-averaged characterization techniques, which obscure the spatiotemporal heterogeneity intrinsic to catalytic surfaces. Single-molecule fluorescence microscopy (SMFM) surmounts this bottleneck by offering nanometer-scale spatial resolution coupled with the capacity to resolve single-turnover events. Herein, we provide a comprehensive overview of the State-of-the-Art applications of fluorogenic probe-coupled SMFM in deciphering the microscopic mechanisms governing photocatalysis. We begin by delineating the operational principles of total internal reflection fluorescence (TIRF) microscopy and categorizing the response mechanisms of three distinct classes of fluorogenic probes: oxidative (e.g., Amplex Red, APF), reductive (e.g., Resazurin, DN-BODIPY), and acidic (e.g., furfuryl alcohol, thiophene) reporters. Subsequently, we highlight seminal studies wherein SMFM has been leveraged to visualize facet-dependent charge separation on model photocatalysts—including TiO_2, BiOBr, and InSe—to map the dynamic activity associated with surface defects and to precisely locate active sites during photoelectrochemical water splitting. Finally, we critically assess the prevailing technical challenges, such as limitations in probe specificity and background interference, while offering a perspective on prospective avenues for methodological refinement. This review is intended to serve as a methodological cornerstone for advancing mechanistic understanding in photocatalysis and for guiding the rational design of high-performance catalysts.

Keywords: single-molecule fluorescence imaging; fluorogenic probe; photocatalysis; reaction mechanism; active site

Check for updates

Received: 19 April 2026
Revised: 28 May 2026
Accepted: 30 May 2026
Published: 1 June 2026

Copyright: © 2026 by the authors. Licensee MDPI, Basel, Switzerland. This article is an open access article distributed under the terms and conditions of the Creative Commons Attribution (CC BY) license.

1. Introduction

Facing the dual challenges of global fossil fuel depletion and worsening greenhouse gas effects, harnessing solar energy to drive catalytic reactions (e.g., water splitting for hydrogen production, carbon dioxide reduction, pollutant degradation) is considered one of the ideal pathways toward sustainable energy and environmental systems [1–9]. Among these, semiconductor photocatalysis has attracted extensive attention due to its potential to directly convert solar energy into chemical energy [10,11]. However, the

practical application of photocatalytic technology remains constrained by low solar-to-chemical energy conversion efficiency, sluggish surface reaction kinetics, and rapid catalyst deactivation [12,13]. The root of these bottlenecks lies in our still-limited understanding of microscopic processes at catalyst surfaces and interfaces, such as photogenerated charge separation, migration, surface reactions, and the dynamic evolution of active sites.

Traditional photocatalysis research heavily relies on ensemble-averaged characterization techniques, including diffuse reflectance spectroscopy, electrochemical impedance spectroscopy, and conventional photocurrent measurements [14,15]. Although these methods provide average performance parameters of catalyst populations, they fundamentally mask the structural and functional heterogeneities that exist among individual catalyst particles or even among different regions of the same particle. Ample evidence indicates that the activity, selectivity, and stability of photocatalysts are closely related to microscopic features, including size, morphology, exposed crystal facets, defect site distribution, and local electronic structure [16–18]. The critical details of these structure–activity relationships are completely smoothed out in ensemble measurements, preventing the precise identification of the active hotspots that truly determine catalytic performance and hindering the rational design of efficient photocatalysts.

To overcome this bottleneck, single-molecule fluorescence microscopy (SMFM) has flourished in recent years and has rapidly become a cutting-edge tool for investigating microscopic photocatalytic mechanisms [19–21]. The core advantage of SMFM lies in its unique spatiotemporal resolution: through single-molecule localization algorithms, its spatial resolution can break the optical diffraction limit to reach 10–50 nm; meanwhile, its millisecond temporal resolution enables real-time capture of single catalytic events (i.e., single turnovers) at individual catalytic sites [22,23]. SMFM operates based on fluorogenic probe molecules. These probes are initially non-fluorescent (or only weakly fluorescent) but undergo a specific chemical transformation (e.g., oxidation or reduction) under the action of photogenerated electrons or holes (or their derived reactive oxygen species) on the photocatalyst surface, thereby turning into a highly fluorescent state [24,25]. Using imaging modes such as total internal reflection fluorescence (TIRF) microscopy, researchers can precisely record the location and time of appearance of each fluorescent product molecule, thereby reconstructing super-resolution activity maps of the catalyst surface. Moreover, through statistical analysis of single-molecule fluorescence time trajectories, key kinetic parameters including reaction rate constants, adsorption equilibrium constants, and intermediate lifetimes can be extracted, providing crucial evidence for elucidating catalytic reaction mechanisms and guiding catalyst design [26–31].

Although several authoritative reviews have systematically summarized the fundamentals and research progress of single-molecule fluorescence imaging in heterogeneous catalysis [26,31,32], existing work still leaves several dimensions to be further deepened. First, the discussion of fluorescent probes has largely remained at the level of qualitative classification based on response mechanisms; a quantitative evaluation framework covering spectral properties, on/off-state quantum yields, multi-dimensional stability, and reaction reversibility has not yet been established, making it difficult to rationally screen and optimize probes according to the requirements of a specific photocatalytic system. Second, most representative reviews were published before 2020 and have not sufficiently integrated the breakthrough advances in frontier areas such as two-dimensional layered semiconductors, plasmonic heterojunctions, and photoelectrochemical water splitting over the past five years (2021–2025). Third, the analysis of technical limitations has mostly focused on experimental operational aspects. At the same time, insufficient attention has been paid to fundamental constraints that restrict the universality of the technique—such as probe photosensitization effects and compatibility with extreme reaction conditions—and

to emerging interdisciplinary directions, including deep-learning-assisted single-molecule localization and high-throughput data analytics, which are rarely discussed.

To address the above issues, this review aims to advance the current understanding from the following three perspectives. First, it establishes a multi-dimensional performance evaluation framework for probes specifically used in single-molecule fluorescence imaging of photocatalysis, clarifying the scientific connotations and quantitative criteria of key parameters, and systematically analyzing the applicable scenarios and inherent limitations of different probes through representative case studies. Second, it comprehensively integrates the core research achievements in this field from 2010 to 2025, with an emphasis on extracting key scientific findings from three major directions: visualization of crystal-face-dependent charge separation, dynamic activity imaging of defect sites, and precise localization of active sites in photoelectrochemical water splitting, thereby revealing the microscopic origin of structural and functional heterogeneity on catalyst surfaces. Third, it provides an in-depth analysis of the main technical bottlenecks currently faced and, in light of cutting-edge advances such as multimodal combination techniques, the development of novel specific probes, and artificial-intelligence-assisted data analysis, proposes forward-looking future development pathways, aiming to offer a methodological reference for a deeper understanding of photocatalytic mechanisms and the rational design of high-performance photocatalysts.

2. Single-Molecule Fluorescence Imaging and Fluorogenic Probes

2.1. Imaging Principle

Single-molecule fluorescence microscopy enables the detection and localization of individual fluorescent molecules in complex photocatalytic systems; its core lies in efficiently suppressing background noise and fully exploiting the photon emission properties of single molecules. Currently, the most commonly used imaging mode in photocatalysis research is total internal reflection fluorescence (TIRF) microscopy [32–35]. The physical basis of TIRF imaging is the evanescent wave generated when total internal reflection occurs at the interface between two media with different refractive indices (Figure 1A). As shown in Figure 1B, when a laser beam strikes the interface from a higher-refractive-index medium (e.g., glass coverslip, $n \approx 1.52$) into a lower-refractive-index medium (e.g., aqueous solution, $n \approx 1.33$) at an angle greater than the critical angle, the light is totally reflected back into the glass, but an electromagnetic field that decays exponentially with distance from the interface, the evanescent wave, exists at the interface. The penetration depth of this evanescent wave is typically only 100–200 nm. Hence, it excites only fluorescent molecules located immediately adjacent to the coverslip surface, while molecules in the bulk solution remain unexcited [36,37]. This characteristic gives TIRF imaging extremely low background fluorescence and a signal-to-noise ratio significantly superior to conventional wide-field (epifluorescence) imaging, thereby allowing reliable detection of emission signals from single fluorescent molecules.

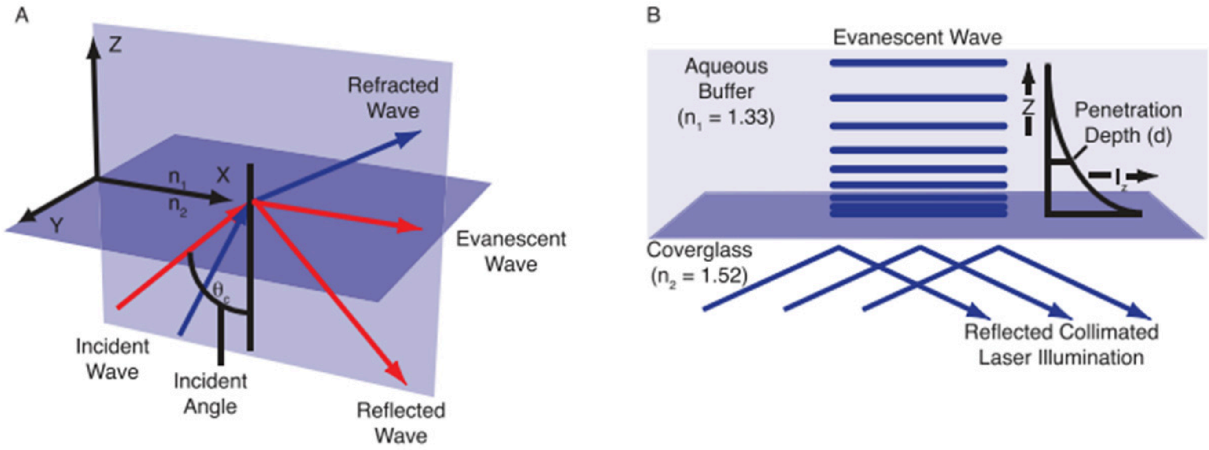


Figure 1. The evanescent wave. (**A**) The incident angle can be described using a coordinate system arranged to display all three orthogonal directions. The x-y plane represents the interface between the glass coverslip and the photocatalytic material. The plane of incidence is the x-z plane, which is parallel to the excitation light beam. (**B**) The evanescent field intensity decays exponentially with increasing distance from the interface. The penetration depth, which is usually between 50 and 300 nm, decreases as the reflection angle grows larger and is dependent on the refractive indices at the interface and the illumination wavelength. Figures (**A**,**B**) are reproduced with permission from ref [38]. Copyright 2022, Wiley Periodicals LLC.

In a typical SMFM experiment, the photocatalyst particles to be studied are sparsely dispersed on a quartz or glass coverslip, above which a microfluidic channel is sealed to a continuous-flow reaction solution containing the fluorogenic probe. An excitation laser (wavelength depends on the probe's excitation peak) is directed through the TIRF objective to generate an evanescent wave at the interface. When a catalytic reaction on the photocatalyst surface converts non-fluorescent (or weakly fluorescent) probe molecules into highly fluorescent products, those product molecules are excited by the evanescent wave and emit fluorescence. The fluorescence signal is collected by the same objective, passes through a dichroic mirror and emission filter, and is recorded by a highly sensitive electron-multiplying charge-coupled device (EMCCD) or scientific complementary metal-oxide-semiconductor (sCMOS) camera [39,40]. The camera exposure time is typically set in the range of 10–100 ms to balance temporal resolution and signal accumulation.

2.2. Classification and Response Mechanisms of Fluorogenic Probes

A key element of SMFM technology is the selection of appropriate fluorogenic probes [41,42]. Depending on the target of detection (photogenerated holes, photogenerated electrons, or reactive oxygen species), researchers have developed a variety of fluorescent probes. Table 1 summarizes the most commonly used probes in current research, and Figure 2 illustrates their molecular structures and schematic response mechanisms.

Table 1. Representative fluorogenic probes for single-molecule fluorescence microscopy (SMFM).

Parameter	Resazurin (Rz)	Amplex Red (AR)	3′-(p-aminophenyl)-fluorescein (APF)	DN-BODIPY	Furfuryl Alcohol (FA)
Initial state	Non-fluorescent (blue-violet)	Weakly fluorescent	Non-fluorescent	Non-fluorescent	Non-fluorescent
Fluorescent product	Resorufin (Rf)	Resorufin (Rf)	Fluorescein	HN-BODIPY	Fluorescent oligomers
Excitation/Emission (nm)	560/585	560/585	490/515	~500/~520	~450–550

Table 1. *Cont.*

Parameter	Resazurin (Rz)	Amplex Red (AR)	3′-(p-aminophenyl)-fluorescein (APF)	DN-BODIPY	Furfuryl Alcohol (FA)
Target species	Photogenerated electrons (e^-) or reducing species	Photogenerated holes (h^+), •OH, H_2O_2	•OH (highly selective, no response to H_2O_2)	Photogenerated electrons (e^-)	Brønsted or Lewis acid sites
Typical application	Imaging reduction reactions (e.g., H_2 reduction, reductive half-reaction in CO oxidation)	Imaging oxidation reactions (e.g., water oxidation, pollutant degradation)	Highly selective imaging of hydroxyl radical generation	Imaging interfacial electron transfer on TiO_2 and other semiconductors	Mapping acid site distribution on solid acid catalysts
Ref.	[43]	[44]	[45]	[46]	[47]

Oxidation-sensitive probes (e.g., Amplex Red (AR), 3′-(p-aminophenyl)-fluorescein (APF)) are typically used to track photogenerated holes or the reactive oxygen species derived from them. AR itself is weakly fluorescent and can be oxidized to strongly fluorescent resorufin (Rf) by horseradish peroxidase or by photogenerated holes/•OH. APF exhibits higher selectivity for •OH and is not directly activated by H_2O_2, thus offering advantages when studying •OH generation pathways during water oxidation. Sambur et al. [48] used single-molecule/single-particle fluorescence imaging with Amplex Red as a model substrate to measure the photoelectrocatalytic oxidation rate on individual rutile TiO_2 nanorods. By systematically analyzing the scaling relationships of reaction rate with light intensity and electrode potential and comparing them with the scaling behavior of photocurrent, this study demonstrated for the first time at the single-particle level that the oxidation of Amplex Red on TiO_2 photoanodes does not occur directly via photogenerated holes but follows an indirect oxidation mechanism mediated by surface-generated hydroxyl radicals (•OH). This work provided direct single-molecule experimental evidence for distinguishing between direct and indirect photocatalytic oxidation pathways and highlighted the unique value of oxidation-sensitive probes in mechanistic discrimination. Zuo et al. [49] used the fluorescent oxidation reaction of Amplex Red as a probe to quantitatively evaluate defect sites on the surface of TiO_2 nanoparticles. They found that the content of Ti^{3+} defect sites was positively correlated with the oxidation activity of Amplex Red, and that additional Ti^{3+} sites could be introduced into commercial TiO_2 by reduction with $NaBH_4$. More importantly, using single-molecule fluorescence imaging, the team successfully mapped the spatial distribution of defect sites within TiO_2 nanowires, revealing significant intra-particle and inter-particle heterogeneity. This work demonstrated that Amplex Red can serve as an effective fluorogenic probe for probing the density of defect sites on semiconductor surfaces. Shen et al. [50] employed the highly selective hydroxyl radical probe APF to image in situ the spatial distribution of •OH generation during photocatalytic water oxidation on individual $W_{18}O_{49}$ nanowires. By colocalizing the spatial distribution of active regions with surface chemical information, this work revealed that ascorbic acid is oxidized during photocatalysis, thereby creating new oxygen vacancies along the nanowire surface. This finding breaks the conventional notion that ligands merely passivate or block active sites; instead, they can dynamically create new active sites through surface redox chemistry. Figure 2 presents single-molecule imaging of photocatalytic reduction and oxidation reactions on bismuth oxybromide (BiOBr) nanoplates using fluorogenic probes. Photogenerated electrons in the conduction band of BiOBr reduce resazurin to the highly fluorescent product resorufin (Figure 2B); meanwhile, photogenerated holes in the valence band oxidize 3′-(p-aminophenyl)-fluorescein (APF) to produce fluorescein (Figure 2E). Subsequently, total internal reflection fluorescence (TIRF) microscopy is employed to image the activation of individual probe molecules on the surface of BiOBr nanoplates (Figure 2C,F). By binning

the single-molecule fluorescence bursts from the surface of a single nanoplate into a grid of 120 nm × 120 nm bins, the activity maps for photocatalytic reduction and oxidation are reconstructed, as shown in Figure 2D and 2G, respectively. Shen et al. [51] simultaneously used Amplex Red (oxidation probe) and Resazurin (reduction probe) on individual BiOBr nanoplates to quantitatively investigate the nanoscale spatial correlation between photocatalytic oxidation and reduction reactions via coordinate-based colocalization analysis. By analyzing the emitted photon counts of the fluorescent probes, this work proposed that defect-rich regions often serve as colocalization centers for both electrons and holes, and that defects promote selective carrier extraction by trapping one type of charge carrier. The above studies systematically illustrate the multi-level applications of oxidation-sensitive fluorescent probes in photocatalytic SMFM: from discriminating reaction mechanisms and localizing defect sites to revealing ligand-mediated dynamic regulation and analyzing the spatial correlation between oxidation and reduction reactions.

Reduction-sensitive probes (e.g., Resazurin (Rz), DN-BODIPY) are used to track photogenerated electrons. Rz is reduced to Rf in an irreversible reaction with high quantum yield, making it the most widely used reduction probe. DN-BODIPY and its water-soluble sulfonated derivatives are more suitable for studying interfacial electron injection processes in semiconductor–metal composite systems. Zhou et al. [52] used the reduction of Resazurin as a model reaction and systematically investigated the catalytic behavior of Au nanoparticles of three sizes (6.0, 9.1, and 13.7 nm) using single-molecule fluorescence microscopy. They found that smaller Au nanoparticles exhibited higher catalytic activity and also showed faster catalytic-induced surface reconstruction rates. In addition, smaller Au nanoparticles displayed higher selectivity between two parallel product dissociation pathways. Figure 2A illustrates the mechanism of hydroxylamine-mediated reduction of resazurin to resorufin catalyzed by Au nanoparticles in aqueous solution. Cao et al. [53] deposited Au nanoparticles on the outer (Au/CNTs-out) and inner (Au/CNTs-in) surfaces of carbon nanotubes and used the Resazurin reduction reaction to investigate the influence of the CNT support on gold catalysis at the single-molecule level. The results showed that Au/CNTs-out had higher intrinsic catalytic activity for product formation; for product dissociation, both supports favored a substrate-assisted dissociation pathway, with faster dissociation on Au/CNTs-out. Li et al. [54] used single-molecule fluorescence microscopy to observe in situ the Resazurin reduction reaction on Ag nanowire–Pd nanoparticle heterostructures. They found that the catalytic activity of Pd nanoparticles was enhanced by approximately 20-fold due to excitation of the localized surface plasmon resonance (LSPR) of the Ag nanowires, with a further enhancement of about 10-fold near roughened Ag nanowires or nanogaps. Ezendam et al. [55] used super-resolution fluorescence microscopy with Resazurin reduction on Au nanorods coated with a porous SiO_2 shell as a model to systematically distinguish multiple plasmonic catalysis mechanisms (electromagnetic field enhancement, thermal effects, hot carrier generation) and their spatial distributions. The study demonstrated that Resazurin reduction can occur through multiple reaction pathways, with different mechanisms exhibiting distinct spatial enhancement patterns that can be distinguished by mapping the spatial distribution of reactivity. Bueno Alejo et al. [56] confirmed from a thermal activation perspective that plasmon excitation of Au nanoparticles can significantly accelerate Resazurin reduction within nanosecond pulses and proposed a cost-effective LED-based strategy for plasmon-assisted catalysis. Furthermore, Zuo et al. [57] encapsulated Au nanorods in a TiO_2 shell (AuNR@TiO_2) and found that the TiO_2 shell effectively separates plasmon-generated hot electron/hole pairs, enhancing Resazurin reduction activity by about 10-fold under 530 nm light excitation. Single-molecule kinetic analysis indicated that the TiO_2 shell not only prolongs charge relaxation times but also introduces additional reaction sites. Wu et al. [58] employed

in situ single-molecule fluorescence microscopy to study carbon nanotube/CdS nanorod one-dimensional-one-dimensional heterostructures for the first time, using Resazurin photoreduction as a probe to quantitatively analyze catalytic activity at different sites. They found that the CdS end bearing the heterojunction exhibited the highest catalytic conversion rate constant, which was 30% higher than that of the middle section, 7% higher than that of the bare CdS end, and 19% higher than that of the CNT end with the heterojunction. Adsorption capacity at different structural sites showed a similar trend, attributed to differences in defect content; for dissociation behavior, direct dissociation dominated on CdS, while substrate-assisted dissociation dominated on CNT. Figure 2I shows the photocatalytic generation of fluorescent HN-BODIPY from non-fluorescent DN-BODIPY on a TiO_2 crystal surface. Tachikawa et al. [59] used the fluorine-generating reaction of DN-BODIPY reduction to HN-BODIPY to reveal, at the single-molecule and single-particle level, differences in photocatalytic activity among different crystal facets of anatase TiO_2 bipyramidal nanoparticles. The study found that the photocatalytic reduction activity of {101} side facets was about four times higher than that of {001} basal facets, and the adsorption equilibrium constants of DN-BODIPY also differed between facets. Through selective UV irradiation, this work also suggested that the {101} facets may act as a "reservoir" for photogenerated electrons. In earlier work from the same group (Tachikawa et al. [60]), the design and synthesis of the DN-BODIPY probe were reported in detail. The probe operates via a photoinduced electron transfer (PET) mechanism, being non-fluorescent in its initial state and becoming strongly fluorescent upon accepting an electron, thereby enabling highly sensitive monitoring of interfacial electron transfer processes on TiO_2 surfaces. These two studies together constitute a complete chain from probe design to application. The above studies demonstrate that the two classes of reduction-sensitive probes, Resazurin and DN-BODIPY, have successfully revealed size effects, support effects, plasmonic enhancement mechanisms, heterojunction site specificity, and facet-dependent charge separation behavior in nanocatalysis at the single-molecule level. These works not only deepen our understanding of the microscopic mechanisms of the photocatalytic reduction half-reaction but also provide single-molecule experimental evidence for the rational design of efficient photocatalysts.

Acid-sensitive fluorescent probes (e.g., furfuryl alcohol (FA), thiophene, styrene derivatives) are important tools for studying heterogeneous acid catalysis using single-molecule fluorescence microscopy. These probe molecules are themselves non-fluorescent but undergo oligomerization or polycondensation reactions catalyzed by Brønsted acid sites to generate strongly fluorescent conjugated species. Roeffaers et al. [61] first used the acid-catalyzed polycondensation of furfuryl alcohol (FA) as a fluorogenic probe, combined with fluorescence microscopy, to track in real time the spatial and temporal dynamics of acid-catalyzed reactions within the pore channels of ZSM-5 zeolite crystals at the single-particle level. This work achieved the first high-spatiotemporal-resolution visualization of Brønsted acid site catalytic activity inside a single zeolite crystal, providing a novel methodological tool for understanding the active site distribution and deactivation mechanisms of heterogeneous acid catalysts. Figure 2H shows the proposed mechanism of chromophore formation during the acid-catalyzed condensation of furfuryl alcohol. Ristanović et al. [62] further combined FA acid-catalyzed oligomerization with three-dimensional single-molecule fluorescence microscopy to quantitatively study the effect of steam treatment on the reactivity of Brønsted acid sites in H-ZSM-5 zeolite crystals at the single-catalytic-turnover level. They found that the single-turnover kinetics of pristine zeolite crystals exhibited significant spatial activity heterogeneity and uncorrelated temporal fluctuations at the nanoscale. Buurmans et al. [63] developed a selective staining method based on the acid-catalyzed oligomerization of thiophene to localize Brønsted acid sites in fluid catalytic cracking (FCC)

catalysts at the single-particle level. Confocal fluorescence microscopy images showed that the zeolite domains within FCC catalyst particles were heterogeneously distributed, and fluorescence intensity (i.e., Brønsted acidity) decreased with increasing degree of deactivation. Whiting et al. [64] extended this method to millimeter-scale ZSM-5/SiO_2 catalyst extrudates to investigate the effect of different Na^+/H^+ exchange levels on the spatial distribution of Brønsted acid sites. They found that partially exchanged extrudates exhibited significant heterogeneity in thiophene oligomer distribution, while fully exchanged samples showed uniform distribution, demonstrating that thiophene probes can be effectively used for quantitative imaging of acid site distribution in industrially sized catalyst particles. Kox et al. [65] combined X-ray absorption, UV/Vis, and confocal fluorescence microspectroscopy to perform chemical imaging of the acid-catalyzed conversion of thiophene derivatives within the micropores of individual coffin-shaped H-ZSM-5 zeolite crystals, revealing significant spatial heterogeneity in the reaction process and successfully correlating the physical structure of the zeolite crystal with its catalytic activity. Recently, Chen et al. [66] used a template-protected alkaline etching method to construct a hierarchical mesoporous system with 2–5 nm pores inside ZSM-5 crystals. Combined with super-resolution fluorescence imaging using a thiophene probe, they found that after alkaline treatment, the mesopore volume increased by 119% and the trimer product density increased by 114%, which were highly correlated with improved diffusion depth of the probe molecules, establishing a clear relationship between pore structure and acid catalytic performance. Ristanović et al. [67] first employed Brønsted acid-catalyzed oligomerization of styrene derivatives as a single-molecule probe to investigate the reactivity of individual H-ZSM-5 zeolite crystals. By forming fluorescent carbenium ions of dimers and trimers with different photostabilities, single-molecule fluorescence microscopy successfully captured the spatial distribution of proton transfer processes inside zeolite crystals. The study found that trimer carbenium ions formed mainly in defect-rich regions of the crystals, providing a new spectroscopic marker for nanoscale quality control of zeolite materials. The above studies demonstrate that the three classes of acid-sensitive probes—furfuryl alcohol, thiophene, and styrene—have successfully achieved spatial localization, activity quantification, and deactivation process tracking of Brønsted acid sites in zeolites and FCC catalysts at the single-particle/single-molecule level. These works not only deepen the understanding of activity heterogeneity and deactivation mechanisms in heterogeneous acid catalysts but also provide single-molecule experimental evidence for the performance evaluation and rational design of industrial catalysts (e.g., FCC catalysts).

It is worth emphasizing that the activation mechanism of a probe must be fully understood when selecting it. For example, AR can be directly oxidized by photogenerated holes or indirectly by •OH, whereas APF responds mainly to •OH. Control experiments (e.g., addition of the •OH quencher DMSO) can distinguish between these two pathways. In addition, the adsorption behavior, photostability, and potential perturbation of the catalytic reaction by the probe molecules themselves must be pre-evaluated.

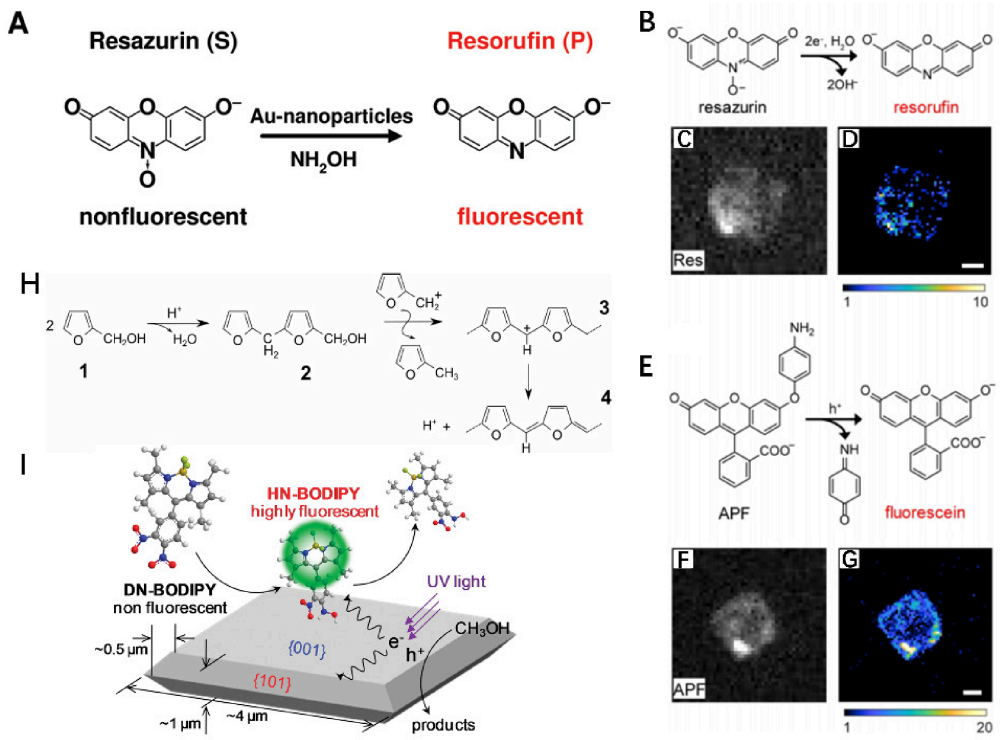


Figure 2. Molecular structures, sensing mechanisms, and schematic illustrations of single-molecule fluorescence imaging for commonly used fluorescent probes. (**A**) Au-nanoparticle-catalyzed reduction of resazurin to resorufin by NH_2OH in aqueous solution. Figure (**A**) is reproduced with permission from ref. [52]. Copyright © 2009 American Chemical Society. (**B**) Reductive deoxygenation of resazurin by photogenerated electrons in BiOBr produces highly fluorescent resorufin. (**C**) Diffraction-limited fluorescence image of a BiOBr nanoplate using resazurin as the fluorogenic probe under dual 405 and 561 nm laser excitation recorded at an exposure time of 50 ms. (**D**) Super-resolution activity map of the nanoplate in panel (**B**) for photocatalytic reduction produced by localizing the positions of all fluorescence bursts. (**E**) Oxidative cleavage of the aminophenyl group of 3′-(p-aminophenyl)-fluorescein (APF) by photogenerated holes in BiOBr produces fluorescein. (**F**) Diffraction-limited fluorescence image of a different BiOBr nanoplate using APF as the fluorogenic probe under dual 405 and 488 nm laser excitation recorded at an exposure time of 50 ms. (**G**) Super-resolution activity map of the nanoplate in panel (**E**) for photocatalytic oxidation produced by localizing the positions of all fluorescence bursts. Color scales: number of fluorescence bursts per bin (120 nm × 120 nm). The white scale bars in panels (**D**,**G**) are 1 µm. Figures (**B**–**G**) are reproduced with permission from ref. [51]. Copyright © 2021 American Chemical Society. (**H**) Proposed formation of chromophores during the acid-catalyzed condensation of furfuryl alcohol. The initial protonation and dimerization of (1) lead to the formation of noncolored bisfurfurylmethyl (2). This molecule undergoes a second hydride transfer, forming a resonance-stabilized carbenium ion (3) and its conjugate structure (4) after a proton loss. Reproduced from ref. [62] under the terms of the CC BY 4.0 license. Copyright © 2015 American Chemical Society. (**I**) Photocatalytic generation of fluorescent HN-BODIPY from non-fluorescent DN-BODIPY over a TiO_2 crystal. Figure (**I**) is reproduced with permission from ref. [59]. Copyright © 2011 American Chemical Society.

2.3. Key Performance Parameters and Design Principles of Fluorogenic Probes

Although the probes described in Section 2.2 (AR, APF, Rz, DN-BODIPY, FA, etc.) have demonstrated powerful capabilities in photocatalytic SMFM studies, their physicochemical properties fundamentally determine the signal-to-noise ratio, spatiotemporal resolution, and reliability of kinetic data. To meet the stringent requirements of single-molecule detection, an ideal fluorogenic probe should generally possess the following key performance parameters.

(a) Stokes shift and excitation/emission wavelengths: The Stokes shift refers to the wavelength difference between the absorption and emission maxima of a probe molecule. A large Stokes shift (typically >80 nm) effectively avoids excitation light scattering and re-absorption, enabling easy separation of the emitted light from the excitation light using dichroic mirrors and bandpass filters, thereby reducing background noise [68]. At the same time, the excitation wavelength should match common commercial lasers (e.g., 405, 488, 532, 561, 640 nm), while the emission wavelength should fall within the high quantum efficiency region of the detector (typically 500–700 nm). Furthermore, the absorption band of the probe should not severely overlap with the intrinsic bandgap absorption of the photocatalyst (e.g., UV absorption of TiO_2) or the plasmonic resonance peaks (e.g., of Au, Ag nanostructures), to avoid photosensitization interference or competitive absorption. For example, DN-BODIPY has excitation/emission maxima at approximately 500/520 nm, matching well with the 488 nm laser, and its reduced product HN-BODIPY exhibits a larger Stokes shift, facilitating rejection of excitation light [46].

(b) Fluorescence quantum yield (dark → bright state): Single-molecule detection requires an extremely low quantum yield for the non-fluorescent (or weakly fluorescent) precursor (the "off" state, typically $\Phi_{dark} < 0.001$) and a high quantum yield for the fluorescent product (the "on" state, $\Phi_{bright} > 0.5$) to achieve maximum signal-to-noise ratio. For instance, resazurin (Rz) itself has a fluorescence quantum yield of approximately 0.003 upon 560 nm excitation, whereas after reduction to resorufin (Rf), the quantum yield increases to about 0.74, improving the signal-to-noise ratio by nearly 250-fold [43]. Similarly, conversion of AR to Rf gives a fluorescence enhancement of about 100-fold [44]. Low background fluorescence is a prerequisite for achieving single-molecule localization precision and is a core feature that distinguishes SMFM from conventional fluorescence microscopy.

(c) Chemical stability, thermal stability, and photostability: Probes must remain chemically inert under the reaction medium (pH, ionic strength, solvent, dissolved oxygen) and experimental temperature (typically 25–80 °C, and even higher for some high-temperature catalytic studies), without nonspecific hydrolysis or auto-oxidation. However, many probes have inherent limitations: AR degrades rapidly at pH > 8.5, the reduction of Rz is competitively inhibited by O_2 [69–73]; FA is stable under strongly acidic conditions but may undergo non-catalytic polymerization at elevated temperatures. Photostability refers to the resistance of the fluorescent product to photobleaching under continuous excitation. Single-molecule fluorescence bursts typically need to be recorded over tens of milliseconds to seconds; if the photobleaching time is too short, insufficient photons will be collected for localization. The use of anti-photobleaching reagents (e.g., Trolox, β-mercaptoethanol) or lower excitation power densities can mitigate the problem, but the best strategy is to design probes with intrinsically high photostability.

(d) Reversible vs. reactive (irreversible) reaction modes: The reaction between a probe and the target species (photogenerated electrons, holes, radicals, or protons) can be classified as irreversible or reversible. Irreversible probes (e.g., Rz → Rf, AR → Rf, APF → fluorescein, DN-BODIPY → HN-BODIPY, FA oligomerization), once activated, lead to stable accumulation of the fluorescent product and are suitable for active-site localization and cumulative activity mapping. Their advantage is that no signal is lost due to reverse reactions; however, they cannot monitor the on/off dynamics of catalytic sites or rapid fluctuations in reaction rates in real time. Reversible probes (e.g., certain probes based on photoinduced electron transfer (PET) or intramolecular charge transfer (ICT)) show enhanced fluorescence in the presence of the target species and return to the dark state after its removal, thus enabling real-time tracking of transient catalytic events [74]. Nevertheless, reversible probes are more difficult to design and often require complex synthesis and calibration. In photocatalytic SMFM studies, the vast majority of applications employ

irreversible probes to obtain highly sensitive time-integrated activity maps. However, for investigating the dynamic deactivation of active sites, charge carrier trapping and release, etc., reversible probes offer irreplaceable advantages.

(e) Probe adsorption and diffusion behavior: The adsorption equilibrium constant (K_{ads}) and surface diffusion coefficient of probe molecules on the catalyst surface directly affect the frequency and residence time of single-molecule fluorescence bursts. Ideally, a probe should exhibit moderate adsorption (K_{ads} in the range of 10^4–10^6 M^{-1}) to ensure sufficiently high surface concentration for capturing catalytic events without blocking active sites or causing local substrate depletion due to overly strong adsorption. Tachikawa et al. [59] found that the K_{ads} of DN-BODIPY on the TiO_2 {101} facet was approximately twice that on the {001} facet, directly contributing to the difference in reduction activity. Moreover, if the diffusion rate of the probe on the surface is much lower than the reaction rate, the spatial distribution of product molecules will reflect the in situ active sites more accurately; conversely, rapid diffusion blurs the activity map. Single-particle tracking (SPT) techniques can directly measure the diffusion coefficient of probes on the catalyst surface, thereby correcting localization errors [75].

In summary, the selection of a fluorogenic probe does not rely solely on response specificity but also requires a comprehensive trade-off among Stokes shift, compatibility of excitation/emission wavelengths with the optical system, quantum yield change, chemical/thermal/photostability, reversible vs. irreversible reaction behavior, and surface adsorption/diffusion characteristics. No current probe satisfies all ideal conditions simultaneously. Researchers should prioritize the various parameters according to the specific photocatalytic reaction system (target species, pH, temperature, illumination wavelength, time resolution requirements) and rigorously validate the reliability of the probe through control experiments (e.g., without catalyst, dark conditions, excitation-wavelength dependence, radical quenching, etc.).

3. Photocatalysts

The catalytic performance of photocatalytic materials is closely related to their exposed crystal facets, surface defects, and charge separation efficiency [76,77]. Conventional ensemble measurements cannot reveal the structural and functional heterogeneity between different regions within a single particle [78–80]. Leveraging its nanoscale spatial resolution and single-turnover kinetic analysis capability, single-molecule fluorescence microscopy has achieved key advances in photocatalysis, including visualization of facet-dependent charge separation pathways, activity imaging and dynamic tracking of defect sites, and precise localization of active sites in photoelectrochemical water splitting.

3.1. Visualization of Facet-Dependent Charge Separation Pathways

Anatase TiO_2, with its well-defined {001} and {101} facets, serves as an ideal model system for such studies. In a pioneering work, Tachikawa et al. [59] used the DN-BODIPY reduction probe to visually demonstrate, for the first time at the single-particle level, the preferential enrichment of photogenerated electrons on the {101} facets. They found that although the {001} facets have higher surface energy, the photocatalytic reduction activity of the {101} facets was approximately four times higher. As shown in Figure 3A, the researchers used a 100 μm pinhole to irradiate UV light onto the central region of the {001} facets of the crystal. In addition to the {001} surface, numerous fluorescence bursts were observed on the unirradiated {101} facets (Figure 3B,D); this pattern was verified on more than five independently tested single crystals. In contrast, when the {101} facets were selectively irradiated with UV light, the catalytic activity on the {001} facets dropped substantially, becoming nearly negligible (Figure 3E). These results indicated that the {101} facets can

serve as storage sites for photogenerated electrons. Subsequent theoretical calculations [81] further supported this model, pointing out that in an aqueous environment, the {101} facets possess the lowest conduction band minimum (CBM), providing a thermodynamic driving force for electron migration. Wang et al. [82] used dual-probe (simultaneously tracking oxidation and reduction) SMFM imaging on decahedral TiO_2 particles and discovered a counterintuitive phenomenon: the highest photocatalytic activity was not found on either flat {001} or {101} facet, but rather concentrated at the edges and corners where the two facets meet. Density functional theory (DFT) calculations revealed that the electronic structure at these geometric discontinuities is reconstructed, forming unique "surface heterojunctions" capable of efficiently capturing both electrons and holes simultaneously. This finding greatly deepens our understanding of active sites on TiO_2, extending the focus from single "facets" to "edges" and "points." Macroscopic photocatalytic experiments by Zheng et al. [83] corroborated this, showing that when TiO_2 microspheres simultaneously expose an appropriate proportion of {001} and {101} facets, they exhibit the highest photocatalytic hydrogen production activity, attributed to the formation of effective charge separation channels between the two facets. Meanwhile, D'Arienzo et al. [84] used electron paramagnetic resonance (EPR) spectroscopy to provide complementary evidence from a defect chemistry perspective, showing that the concentrations of photogenerated Ti^{3+} (electron centers) and O^- (hole centers) are positively correlated with the exposed areas of {101} and {001} facets, respectively, further reinforcing the connection between specific facets and particular charge trapping sites. The facet-dependent charge separation effect is also significant in the $BiVO_4$ system but exhibits more complex characteristics. Banik et al. [85] used scanning photoelectrochemical microscopy (SPCM) to image individual $BiVO_4$ particles and confirmed that the lateral {110} facets generally exhibit higher photocurrent than the top {010} facets. Surprisingly, they observed significant photocurrent differences even among different {110} facets on the same particle, indicating that besides facet orientation, the specific surface chemical environment (e.g., defects, terminating atoms) is also critically important. This finding reminds us that simply attributing activity to a particular facet is an oversimplification; the microscopic heterogeneity of surface chemistry is an indispensable key variable. Zhu et al. [86] used spatially resolved surface photovoltage spectroscopy to directly observe up to a 70-fold difference in photovoltage signals between the {011} and {010} facets on a single $BiVO_4$ particle, providing direct electrical evidence for facet-dependent charge separation. SMFM and related imaging studies on model semiconductors such as TiO_2 and $BiVO_4$ have clearly established the fundamental physical picture of facet-dependent charge separation, where {101}/{001} facets serve as reduction/oxidation sites, respectively, providing an important first-principles basis for understanding photocatalytic processes. However, recent research has shifted the focus from simple "facets" to finer "interfacial junctions" and "surface defects," indicating that the nature of catalytic active sites is more dynamic and complex.

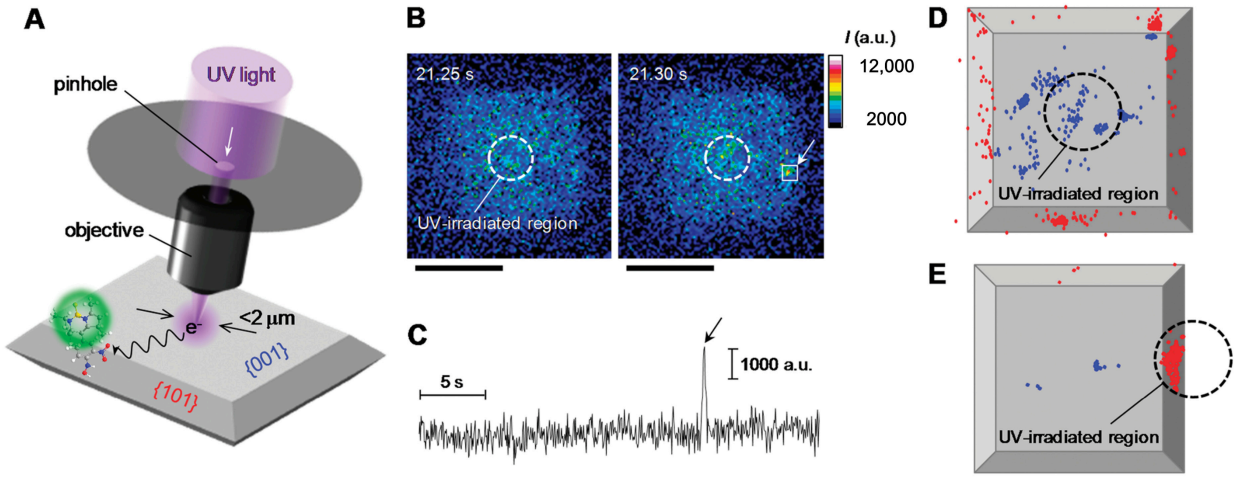


Figure 3. (**A**) Illustration of the remote photocatalytic reaction on the {101} facets with DN-BODIPY during photoirradiation onto the {001} facets. The irradiated area was limited by a pinhole (the spot diameter is 2 μm on the crystal surface). (**B**) Fluorescence image of a TiO_2 crystal that is immobilized on the cover glass in Ar-saturated DN-BODIPY solution (1.0 μM, in methanol) under a 488 nm laser and UV irradiation. The scale bars are 4 μm. (**C**) Time trace of fluorescence intensity observed over the square region in panel (**B**) (see the arrow). The UV irradiation area is inside the white circle in the images. (**D**,**E**) Location of fluorescence bursts on the {001} (blue) and {101} (red) facets. The UV irradiation areas are inside the black circles (diameter 2 μm). Figures (**A**–**E**) are reproduced with permission from ref. [59]. Copyright © 2011 American Chemical Society.

3.2. Activity Mapping and Dynamic Chemistry of Defect Sites

Defects (e.g., oxygen vacancies) play a "double-edged sword" role in photocatalysis. Shen et al. [43] used the Resazurin reduction probe to monitor in situ the dynamic changes in catalytic activity during the photoinduced formation of oxygen vacancies on individual BiOBr nanoplates: low concentrations of oxygen vacancies enhanced visible light absorption and increased activity, whereas high concentrations introduced recombination centers and weakened probe adsorption, leading to decreased activity—providing the first experimental verification at the single-particle level of the "activation-deactivation" mechanism of oxygen vacancies. In the same system, Shen et al. [51] simultaneously used APF (oxidation) and Resazurin (reduction) dual probes for coordinate-based colocalization analysis. They found that the same batch of BiOBr nanoplates could be divided into two types: in one type, oxidation and reduction reactions were spatially uncorrelated (defect-rich regions selectively trapped a single carrier type), while in the other type, the two reactions were highly colocalized in defect-poor regions, and the colocalized regions exhibited significantly higher oxidation activity and fluorescence photon counts. As shown in Figure 4, after separately imaging the oxidation reaction (APF probe) and reduction reaction (resazurin probe) on the same nanoplate (Figure 4a,b), the CBC algorithm was used to calculate the spatial proximity of each reaction site to the other type of reaction site (Figure 4c–f), ultimately revealing two distinct behaviors: "site segregation" and "site colocalization." This work revealed that defect-poor regions are key to achieving sacrificial-agent-free overall water splitting. Shen et al. [87] used dual-probe colocalization of APF and furfuryl alcohol on $W_{18}O_{49}$ nanowires to demonstrate that the most active regions for hydroxyl radical generation also had the highest oxygen vacancy density and that blocking oxygen vacancy accessibility by chemical modification significantly decreased activity. Compared with three-dimensional bulk materials, two-dimensional layered semiconductors have almost fully exposed surfaces, making them ideal platforms for studying the relationship between defect structure and activity. The study by Huang et al. [88] on two-dimensional InSe thin layers is exemplary. Using SMFM, they quantitatively determined the catalytic activity of

four typical structural features—basal plane, edges, wrinkles, and vacancies—on the same InSe flake. The results revealed a clear activity order: vacancies > wrinkles > edges > basal plane, with the intrinsic activity of a single vacancy being about 10.5 times that of the basal plane. Deeper analysis revealed a trade-off between "adsorption" and "reaction" at different sites: the flat basal plane had the strongest substrate adsorption capacity (molecules can lie flat) but the slowest reaction rate, whereas vacancies had weaker adsorption but the fastest conversion rate. Wu et al. [89] further combined SMFM with femtosecond interferometric scattering microscopy (Femto-iSCAT) to establish a nanoscale correlation between photocatalytic activity and charge carrier lifetime at different sites on InSe, finding that the specific reaction rate was positively and linearly correlated with carrier lifetime but weakly correlated with carrier concentration, providing clearer carrier dynamics guidance for defect engineering. Through detailed SMFM studies on BiOBr, $W_{18}O_{49}$, InSe, and other materials, we recognize that defects are no longer simple binary labels of "active site" or "recombination center." They possess unique electronic structures, spatial distributions, and dynamic behaviors that profoundly regulate every step of photocatalysis.

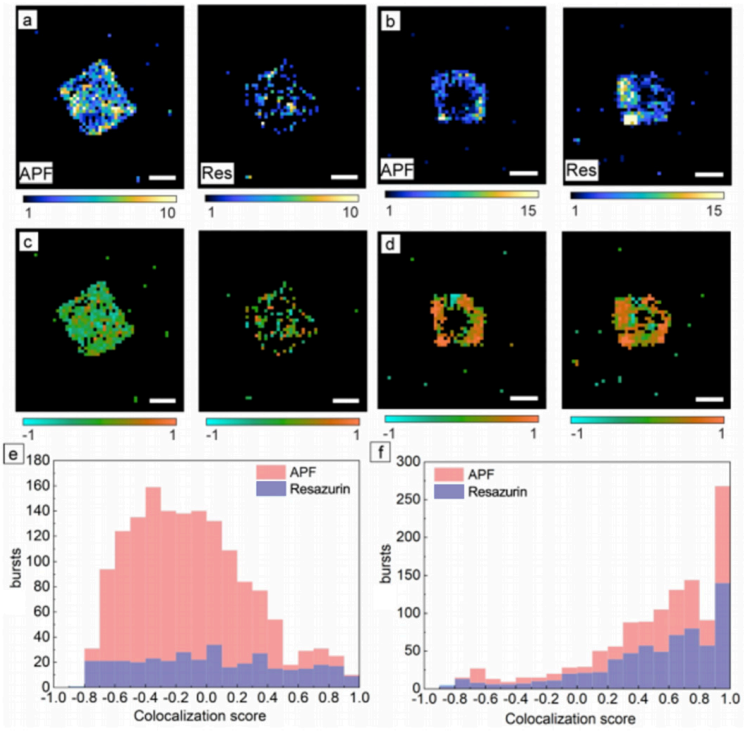


Figure 4. Colocalization of photocatalytic oxidation and reduction reactions on representative type I (**a**,**c**,**e**) and type II (**b**,**d**,**f**) BiOBr nanoplates. (**a**,**b**) Super-resolution activity maps of two BiOBr nanoplates using APF (1st and 3rd columns) and resazurin (2nd and 4th columns) as probes for photocatalytic oxidation and reduction, respectively. Color scale: number of fluorescence bursts per bin (120 nm × 120 nm). (**c**,**d**) Coordinate-based colocalization (CBC) maps for fluorescence bursts using APF (1st and 3rd columns) and resazurin (2nd and 4th columns). Color scale: median CBC score in each bin ranging from −1 for anticorrelated to +1 for perfectly correlated burst distributions. All white scale bars are 1 µm. (**e**,**f**) Distribution of CBC scores for APF (red) and resazurin (blue) bursts showing low spatial correlation for the type I nanoplate in panel (**e**) and high spatial correlation for the type II nanoplate in panel (**f**). Figures (**a**–**f**) are reproduced with permission from ref. [51]. Copyright © 2021 American Chemical Society.

3.3. Precise Localization of Active Sites in Photoelectrochemical Water Splitting

Sambur et al. [90] combined super-resolution single-molecule fluorescence imaging with sub-particle photocurrent measurements to simultaneously map electron-driven and

hole-driven reaction activity on individual TiO_2 nanorods. They found that the most active sites for water oxidation were also the sites with the most severe electron-hole recombination. Guided by the activity maps, they achieved site-selective deposition of cocatalysts and found that depositing cocatalysts on low-activity sites most significantly increased the photocurrent, while deposition at sites with a positive onset potential was most effective for reducing the overpotential. They proposed a "block-deposit-remove" strategy that increased the overall photocurrent by 60% and shifted the onset potential negatively by 70 mV. Sambur et al. [91] further tracked the surface concentration of Ti–OH• intermediates on TiO_2 photoanodes and correlated it with photocurrent, revealing the potential dependence of the interfacial hole transfer and O–O bond formation rate constants. Okazaki et al. [92] achieved site-selective deposition of a CoO_x cocatalyst at the edges of Au nanoparticles on a plasmonic Au/TiO_2 photoanode, resulting in an approximately three-fold increase in photocurrent. Hirayama et al. [93] developed a facet-selective ultra-fine cocatalyst loading method, selectively depositing approximately 1 nm Rh-Cr mixed oxide on the {100} facets of $SrTiO_3/Al$, achieving the highest apparent quantum yield reported to date.

In summary, the above studies—from facet-dependent charge separation, dynamic and spatial heterogeneity of defect sites, to precise localization of active sites and cocatalyst engineering in photoelectrochemical water splitting—systematically demonstrate the powerful capabilities of single-molecule fluorescence imaging and related techniques in probing the microscopic mechanisms of semiconductor photocatalysis.

4. Challenges and Outlook

After nearly two decades of development, single-molecule fluorescence microscopy (SMFM) has expanded from initial model reaction studies to complex photocatalytic materials, heterojunction interfaces, and even bio-inorganic hybrid systems, achieving fruitful results in revealing active site distribution, charge separation pathways, and reaction kinetics. Nevertheless, the widespread application of this technique still faces several fundamental challenges. In recent years, researchers have made important progress in overcoming these bottlenecks, and new imaging modalities are continuously broadening the application boundaries of SMFM.

Most existing probes perform best in neutral aqueous buffers and have limited compatibility with industrially relevant conditions such as strong acids/bases, high temperatures/pressures, and gas-phase reactions. Amplex Red is unstable at pH > 8.5, and the reduction of Resazurin is inhibited in the presence of oxygen [69–73]. This means that the vast majority of SMFM experiments are confined to the narrow pH window of 6–8 (typically pH 7.4 phosphate buffer). This limitation is critical for photocatalysis research. Many important photocatalytic reactions, such as CO_2 reduction, nitrate reduction, and organic pollutant degradation, often have optimal reaction conditions in acidic or alkaline environments. For example, photoelectrocatalytic CO_2 reduction [94–96] is often carried out in $KHCO_3$ or CO_2-saturated acidic electrolytes, with pH values far below the working range of the probes. Similarly, water oxidation is more favorable at high pH, but AR rapidly degrades under those conditions. An often overlooked issue is the photosensitization effect of probe molecules [97]. Many fluorescent probes (including AR, APF, and Rz) have significant absorption in the visible region. Under SMFM excitation light (e.g., 488 nm, 532 nm, or 561 nm), the probe molecules themselves may be excited and inject electrons into the conduction band of the semiconductor—a process identical to the working principle of dye-sensitized solar cells. In this case, the probe no longer "reports" photocatalytic activity but rather "drives" the photocatalytic reaction. Distinguishing between "photocatalysis" and "photosensitization" requires rigorous control experiments without catalysts and with

different excitation wavelengths, a point that has not received sufficient attention in many published works.

Developing fluorescent probes suitable for strong acids/bases, organic solvents, high temperatures/pressures, and gas-phase reaction conditions is the top priority for broadening the application scope of SMFM. Recently developed specific probes for CO, NO_2^-, NH_3, etc., offer new possibilities for in situ imaging of photocatalytic CO_2 reduction, N_2 fixation, and other reactions. Combining SMFM with ultrafast spectroscopy, tip-enhanced Raman spectroscopy (TERS) [98], in situ transmission electron microscopy (TEM)/X-ray absorption spectroscopy (XAS) [99,100], and other techniques is expected to simultaneously obtain multi-dimensional information (activity maps, electronic structure, chemical composition, atomic structure) on the same catalyst particle, truly enabling a direct "structure-activity" correlation. The application of deep learning in single-molecule localization is advancing rapidly; frameworks such as LiteLoc [101] enable end-to-end high-precision localization and real-time data analysis. In the future, machine-learning-assisted automated data analysis pipelines will turn SMFM into a high-throughput, high-precision platform for catalysis research. At the same time, applying SMFM to single-atom catalysts to resolve the intrinsic activity and dynamic evolution of individual metal sites at the single-atom level, as well as developing in situ imaging setups suitable for high-temperature, high-pressure, and gas-phase reactions, will bring SMFM closer to real industrial catalytic conditions and promote the translation of fundamental research toward practical applications.

5. Conclusions

Semiconductor photocatalysis, as an important approach to addressing global energy crises and environmental pollution, has long been constrained by insufficient understanding of the microscopic processes at surfaces and interfaces. Traditional ensemble-averaged characterization methods cannot reveal the structural and functional heterogeneity of catalyst surfaces, obscuring the active sites and reaction pathways that truly determine catalytic performance. Single-molecule fluorescence microscopy, with its nanoscale spatial resolution and millisecond temporal resolution, overcomes the dual limitations of the optical diffraction limit and ensemble averaging, enabling in situ, real-time observation of individual catalyst particles, individual active sites, and even single catalytic turnover events. This represents a revolutionary breakthrough for investigating microscopic photocatalytic mechanisms. In summary, this review provides a comprehensive methodological framework for single-molecule studies of photocatalytic surface and interface processes by establishing a systematic performance evaluation system for fluorescent probes, comprehensively integrating cutting-edge research findings from the past five years, and conducting an in-depth analysis of the bottlenecks hindering technological translation. Looking forward, with the development of novel functional probes, the integration of multimodal imaging techniques, and the deeper involvement of artificial intelligence, single-molecule fluorescence imaging is poised to play an irreplaceable role in unveiling the dynamic reaction mechanisms of photocatalysis and guiding the rational design of high-performance catalysts.

Author Contributions: Z.Y.: Conceptualization, methodology, investigation, data curation, writing—original draft, visualization. X.S.: Conceptualization, investigation, data curation, writing—original draft, writing—review and editing. Y.N.: Investigation, data curation, formal analysis, writing—review and editing, visualization. C.S. and Y.S.: Resources, supervision, writing—review and editing, validation. Y.L.: Conceptualization, supervision, project administration, funding acquisition, writing—review and editing, final approval of manuscript. All authors have read and agreed to the published version of the manuscript.

Funding: This work has been supported by the Department of Scientific Research project in Heilongjiang province (No: PL2024H010), the 2024 Heilongjiang Provincial Colleges and Universities

Fundamental Scientific Research Business Funds Scientific Research Project (No: 2024-KYYWF-0583), and the "Research and development team of northern unique medicinal resources", Jiamusi University "East Pole" academic team (Team No: DJXSTD202403).

Institutional Review Board Statement: Not applicable.

Informed Consent Statement: Not applicable.

Data Availability Statement: No new data were created or analyzed in this study.

Conflicts of Interest: The authors declare no conflicts of interest.

References

1. Hota, P.; Das, A.; Maiti, D.K. A short review on generation of green fuel hydrogen through water splitting. *Int. J. Hydrogen Energy* **2023**, *48*, 523–541. [CrossRef]
2. Zhao, W.; Chen, Z.; Yang, X.; Qian, X.; Liu, C.; Zhou, D.; Sun, T.; Zhang, M.; Wei, G.; Dissanayake, P.D.; et al. Recent advances in photocatalytic hydrogen evolution with high-performance catalysts without precious metals. *Renew. Sustain. Energy Rev.* **2020**, *132*, 110040. [CrossRef]
3. Zhu, J.; Hu, L.; Zhao, P.; Lee, L.Y.S.; Wong, K.Y. Recent advances in electrocatalytic hydrogen evolution using nanoparticles. *Chem. Rev.* **2019**, *120*, 851–918. [CrossRef]
4. Zhang, Z.; Pan, S.Y.; Li, H.; Cai, J.; Olabi, A.G.; Anthony, E.J.; Manovic, V. Recent advances in carbon dioxide utilization. *Renew. Sustain. Energy Rev.* **2020**, *125*, 109799. [CrossRef]
5. Liang, X.; Ke, Q.; Zhao, X.; Chen, X. Graphene-supported tin single-atom catalysts for CO_2 hydrogenation to HCOOH: A theoretical investigation of performance under different N coordination numbers. *ACS Appl. Nano Mater.* **2023**, *6*, 4489–4498. [CrossRef]
6. Shaheen, S.; Ali, S.A.; Mir, U.F.; Sadiq, I.; Ahmad, T. Recent advances in transition metal phosphide nanocatalysts for H_2 evolution and CO_2 reduction. *Catalysts* **2023**, *13*, 1046. [CrossRef]
7. Smith, P.T.; Benke, B.P.; Cao, Z.; Kim, Y.; Nichols, E.M.; Kim, K.; Chang, C.J. Iron porphyrins embedded into a supramolecular porous organic cage for electrochemical CO_2 reduction in water. *Angew. Chem. Int. Ed.* **2018**, *130*, 9832–9836. [CrossRef]
8. Bekele, T.; Alamnie, G. The photocatalytic degradation of organic pollutants-a comprehensive overview. *Results Chem.* **2025**, *18*, 102758. [CrossRef]
9. Yu, Y.; Qiao, Z.; Ding, C. Built-In Electric Field Boost Photocatalytic Degradation of Pollutants in Wastewater. *Chem. Rec.* **2024**, *24*, e202400106. [CrossRef]
10. Zhang, L.; Jaroniec, M. Toward designing semiconductor-semiconductor heterojunctions for photocatalytic applications. *Appl. Surf. Sci.* **2018**, *430*, 2–17. [CrossRef]
11. Huang, F.; Zhang, F.; Wang, Y.; Lang, X. Semiconductor cooperative photocatalysis with TEMPO. *Trends Chem.* **2024**, *6*, 115–127. [CrossRef]
12. Zhang, F.; Wang, X.; Liu, H.; Liu, C.; Wan, Y.; Long, Y.; Cai, Z. Recent advances and applications of semiconductor photocatalytic technology. *Appl. Sci.* **2019**, *9*, 2489. [CrossRef]
13. Zhang, W.; Huang, W.; Wu, B.; Yang, J.; Jin, J.; Zhang, S. Excitonic effect in MOFs-mediated photocatalysis: Phenomenon, characterization techniques and regulation strategies. *Coord. Chem. Rev.* **2023**, *491*, 215235. [CrossRef]
14. RamezaniSani, S.; Rajabi, M.; Mohseni, F. Influence of nitrogen doping on visible light photocatalytic activity of TiO_2 nanowires with anatase-rutile junction. *Chem. Phys. Lett.* **2020**, *744*, 137217. [CrossRef]
15. Tie, W.; Jin, J.; Bhattacharyya, S.S.; Yue, H.; Lei, Y.; Zheng, Z.; He, W.; Lee, S.H. Covalent bonding of ZnO nanostructures with dispersible carbon nanotubes for self-assembly photocatalytic heterostructures. *Appl. Surf. Sci.* **2019**, *492*, 219–227. [CrossRef]
16. Zhong, B.; Li, S.; Hu, J.; Yang, X.; Cai, Y.; Li, C.M.; Qu, J. Advances in ultrasound-assisted photocatalyst synthesis and piezo-photocatalysts. *J. Mater. Chem. A* **2023**, *11*, 22608–22630. [CrossRef]
17. Luo, Y.; Wang, X.; Gao, F.; Jiang, L.; Wang, D.; Pan, H. From single atom photocatalysts to synergistic photocatalysts: Design principles and applications. *Adv. Funct. Mater.* **2025**, *35*, 2418427. [CrossRef]
18. Ullah, S.; Ferreira-Neto, E.P.; Khan, A.A.; Medeiros, I.P.M.; Wender, H. Supported nanostructured photocatalysts: The role of support-photocatalyst interactions. *Photochem. Photobiol. Sci.* **2023**, *22*, 219–240. [CrossRef]
19. Hendriks, F.C.; Meirer, F.; Kubarev, A.V.; Ristanović, Z.; Roeffaers, M.B.J.; Vogt, E.T.C.; Bruijnincx, P.C.A.; Weckhuysen, B.M. Single-molecule fluorescence microscopy reveals local diffusion coefficients in the pore network of an individual catalyst particle. *J. Am. Chem. Soc.* **2017**, *139*, 13632–13635. [CrossRef]
20. Hendriks, F.C.; Mohammadian, S.; Ristanović, Z.; Kalirai, S.; Meirer, F.; Vogt, E.T.C.; Bruijnincx, P.C.A.; Gerritsen, H.C.; Weckhuysen, B.M. Integrated transmission electron and single-molecule fluorescence microscopy correlates reactivity with ultrastructure in a single catalyst particle. *Angew. Chem. Int. Ed.* **2018**, *130*, 263–267. [CrossRef]

21. Blum, S.A. Location change method for imaging chemical reactivity and catalysis with single-molecule and-particle fluorescence microscopy. *Phys. Chem. Chem. Phys.* **2014**, *16*, 16333–16339. [CrossRef]
22. Dunn, B.C.; Valdez, S.; Qiang, Z. Single-molecule fluorescence microscopy for imaging chemical reactions: Recent progress and future opportunities for advancing polymer systems. *J. Polym. Sci.* **2023**, *62*, 1235–1259. [CrossRef]
23. Breton, V.; Nazac, P.; Boulet, D.; Danglot, L. Molecular mapping of neuronal architecture using STORM microscopy and new fluorescent probes for SMLM imaging. *Neurophotonics* **2024**, *11*, 014414. [CrossRef] [PubMed]
24. Tian, R.; Yu, Q.; Mei, L.J.; Zhu, F.Y.; Qin, Q.; Ma, R.; Wang, Y.L.; Li, C.; Zhu, M.Q. Single-molecule multi-target fluorescent imaging for latent fingerprints based on aggregation-induced emission. *Sens. Actuators B Chem.* **2023**, *396*, 134634. [CrossRef]
25. Cao, J.; Zhang, D.; Xu, W. Imaging the electrochemical reactions on single-particle by single-molecule fluorescent microscopy. *Curr. Opin. Electrochem.* **2023**, *41*, 101360. [CrossRef]
26. Yan, C.; Mei, X.; Gong, X.; Xu, W. Practical applications of total internal reflection fluorescence microscopy for nanocatalysis. *Ind. Chem. Mater.* **2024**, *2*, 85–99. [CrossRef]
27. Uddin, S.Z.; Talukder, M.A. Two-dimensional materials for improved resolution in total internal reflection fluorescence microscopy. *Mater. Res. Express* **2017**, *4*, 096203. [CrossRef]
28. Fu, B.; Flynn, J.D.; Isaacoff, B.P.; Rowland, D.J.; Biteen, J.S. Super-resolving the distance-dependent plasmon-enhanced fluorescence of single dye and fluorescent protein molecules. *J. Phys. Chem. C* **2015**, *119*, 19350–19358. [CrossRef]
29. Easter, Q.T.; Blum, S.A. Organic and organometallic chemistry at the single-molecule,-particle, and-molecular-catalyst-turnover level by fluorescence microscopy. *Acc. Chem. Res.* **2019**, *52*, 2244–2255. [CrossRef]
30. Hwang, S.; Chen, X.; Zhou, G.; Su, D. In situ transmission electron microscopy on energy-related catalysis. *Adv. Energy Mater.* **2020**, *10*, 1902105. [CrossRef]
31. Janssen, K.P.F.; De Cremer, G.; Neely, R.K.; Kubarev, A.V.; Van Loon, J.; Martens, J.A.; De Vos, D.E.; Roeffaers, M.B.J.; Hofkens, J. Single molecule methods for the study of catalysis: From enzymes to heterogeneous catalysts. *Chem. Soc. Rev.* **2014**, *43*, 990–1006. [CrossRef]
32. Chen, T.; Dong, B.; Chen, K.; Zhao, F.; Cheng, X.; Ma, C.; Lee, S.; Zhang, P.; Kang, S.H.; Ha, J.W.; et al. Optical super-resolution imaging of surface reactions. *Chem. Rev.* **2017**, *117*, 7510–7537. [CrossRef]
33. Li, Y.; Ning, X.; Ma, Q.; Qin, D.; Lu, X. Recent advances in electrochemistry by scanning electrochemical microscopy. *TrAC Trends Anal. Chem.* **2016**, *80*, 242–254. [CrossRef]
34. Lin, Y.; Zhou, M.; Tai, X.; Li, H.; Han, X.; Yu, J. Analytical transmission electron microscopy for emerging advanced materials. *Matter* **2021**, *4*, 2309–2339. [CrossRef]
35. Dai, S.; Yan, X.; Gao, W.; Tieu, P.; Graham, G.W.; Pan, X. Transmission Electron Microscopy of Catalytic Nanomaterials at Atomic Resolution. *Microsc. Microanal.* **2019**, *25*, 2054–2055. [CrossRef]
36. Ha, T.; Enderle, T.; Ogletree, D.F.; Chemla, D.S.; Selvin, P.R.; Weiss, S. Probing the interaction between two single molecules: Fluorescence resonance energy transfer between a single donor and a single acceptor. *Proc. Natl. Acad. Sci. USA* **1996**, *93*, 6264–6268. [CrossRef]
37. Jung, G.; Schmitt, A.; Jacob, M.; Hinkeldey, B. Fluorescent Probes for Chemical Transformations on the Single-Molecule Level. *Ann. N. Y. Acad. Sci.* **2008**, *1130*, 131–137. [CrossRef] [PubMed]
38. Fish, K.N. Total internal reflection fluorescence (TIRF) microscopy. *Curr. Protoc.* **2022**, *2*, e517. [CrossRef] [PubMed]
39. Lin, R.; Clowsley, A.; Baddeley, D.; Jayasinghe, I.; Soeller, C. Single Molecule Localisation Microscopy with sCMOS Cameras. *Biophys. J.* **2016**, *110*, 161a–162a. [CrossRef]
40. Mandracchia, B.; Zheng, C.; Rajendran, S.; Liu, W.; Forghani, P.; Xu, C.; Jia, S. High-speed optical imaging with sCMOS pixel reassignment. *Nat. Commun.* **2024**, *15*, 4598. [CrossRef]
41. von Diezmann, L.; Shechtman, Y.; Moerner, W.E. Three-dimensional localization of single molecules for super-resolution imaging and single-particle tracking. *Chem. Rev.* **2017**, *117*, 7244–7275. [CrossRef]
42. Zaza, C.; Chiarelli, G.; Zweifel, L.P.; Pilo-Pais, M.; Sisamakis, E.; Barachati, F.; Stefani, F.D.; Acuna, G.P. Super-resolved FRET imaging by confocal fluorescence-lifetime single-molecule localization microscopy. *Small Methods* **2023**, *7*, 2201565. [CrossRef]
43. Shen, M.; Ding, T.; Luo, J.; Tan, C.; Mahmood, K.; Wang, Z.; Zhang, D.; Mishra, R.; Lew, M.D.; Sadtler, B. Competing activation and deactivation mechanisms in photodoped bismuth oxybromide nanoplates probed by single-molecule fluorescence imaging. *J. Phys. Chem. Lett.* **2020**, *11*, 5219–5227. [CrossRef]
44. Goertz, J.P.; White, I.M. Peroxidyme-Amplified Radical Chain Reaction (PARCR): Visible Detection of a Catalytic Reporter. *Angew. Chem. Int. Ed.* **2017**, *56*, 13411–13415. [CrossRef]
45. Dickinson, B.C.; Huynh, C.; Chang, C.J. A palette of fluorescent probes with varying emission colors for imaging hydrogen peroxide signaling in living cells. *J. Am. Chem. Soc.* **2010**, *132*, 5906–5915. [CrossRef] [PubMed]
46. Irmler, P.; Winter, R.F. Complexes trans-Pt (BODIPY) X (PEt 3) 2, excitation energy-dependent fluorescence and phosphorescence emissions, oxygen sensing and photocatalysis. *Dalton Trans.* **2016**, *45*, 10420–10434. [CrossRef]

47. Dou, K.; Chen, G.; Yu, F.; Liu, Y.; Chen, L.; Cao, Z.; Chen, T.; Li, Y.; You, J. Bright and sensitive ratiometric fluorescent probe enabling endogenous FA imaging and mechanistic exploration of indirect oxidative damage due to FA in various living systems. *Chem. Sci.* **2017**, *8*, 7851–7861. [CrossRef] [PubMed]
48. Sambur, J.B.; Chen, P. Distinguishing direct and indirect photoelectrocatalytic oxidation mechanisms using quantitative single-molecule reaction imaging and photocurrent measurements. *J. Phys. Chem. C* **2016**, *120*, 20668–20676. [CrossRef]
49. Zuo, L.; Hossain, M.A.; Dubadi, R.; Kist, M.M.; Farhana, F.; Chen, J.; Jaroniec, M.; Shen, H. Fluorogenic Reaction Probes Defect Sites on Titanium Dioxide Nanoparticles. *ChemNanoMat* **2024**, *10*, e202400031. [CrossRef]
50. Shen, M.; Ding, T.; Tan, C.; Rackers, W.H.; Zhang, D.; Lew, M.D.; Sadtler, B. In situ imaging of catalytic reactions on tungsten oxide nanowires connects surface–ligand redox chemistry with photocatalytic activity. *Nano Lett.* **2022**, *22*, 4694–4701. [CrossRef]
51. Shen, M.; Ding, T.; Rackers, W.H.; Tan, C.; Mahmood, K.; Lew, M.D.; Sadtler, B. Single-molecule colocalization of redox reactions on semiconductor photocatalysts connects surface heterogeneity and charge-carrier separation in bismuth oxybromide. *J. Am. Chem. Soc.* **2021**, *143*, 11393–11403. [CrossRef]
52. Zhou, X.; Xu, W.; Liu, G.; Panda, D.; Chen, P. Size-dependent catalytic activity and dynamics of gold nanoparticles at the single-molecule level. *J. Am. Chem. Soc.* **2010**, *132*, 138–146. [CrossRef]
53. Cao, Y.; Kang, S.H. Single-Molecule Nanocatalysis Via the Support Effect of Gold Nanoparticles on Carbon Nanotubes. *Bull. Korean Chem. Soc.* **2019**, *40*, 14–19. [CrossRef]
54. Li, Z.; Devasenathipathy, R.; Wang, J.; Yu, L.; Liang, Y.; Sheng, H.; Zhu, Y.; Li, H.; Uji-i, H.; Huang, X.; et al. Direct observation of the plasmon-enhanced palladium catalysis with single-molecule fluorescence microscopy. *Nano Res.* **2023**, *16*, 8817–8826. [CrossRef]
55. Ezendam, S.; Gargiulo, J.; Sousa-Castillo, A.; Lee, J.B.; Nam, Y.S.; Maier, S.A.; Cortés, E. Spatial distributions of single-molecule reactivity in plasmonic catalysis. *ACS Nano* **2023**, *18*, 451–460. [CrossRef]
56. Alejo, C.J.B.; Fasciani, C.; Grenier, M.; Netto-Ferreira, J.C.; Scaiano, J.C. Reduction of resazurin to resorufin catalyzed by gold nanoparticles: Dramatic reaction acceleration by laser or LED plasmon excitation. *Catal. Sci. Technol.* **2011**, *1*, 1506–1511. [CrossRef]
57. Zuo, L.; King, H.; Hossain, M.A.; Farhana, F.; Kist, M.M.; Stratton, R.L.; Chen, J.; Shen, H. Single-molecule spectroscopy reveals the plasmon-assisted nanozyme catalysis on AuNR @ TiO_2. *Chem. Biomed. Imaging* **2023**, *1*, 760–766. [CrossRef] [PubMed]
58. Wu, S.; Lee, J.K.; Tan, J.W.E.; Chan, J.X.; Xu, R.; Zhang, Z. In Situ Quantitative Study of Single-Molecule Photoreduction Activities and Kinetics on 1D–1D Heterostructure. *Small* **2024**, *20*, 2307057. [CrossRef]
59. Tachikawa, T.; Yamashita, S.; Majima, T. Evidence for crystal-face-dependent TiO_2 photocatalysis from single-molecule imaging and kinetic analysis. *J. Am. Chem. Soc.* **2011**, *133*, 7197–7204. [CrossRef]
60. Tachikawa, T.; Wang, N.; Yamashita, S.; Cui, S.C.; Majima, T. Design of a highly sensitive fluorescent probe for interfacial electron transfer on a TiO_2 surface. *Angew. Chem. Int. Ed.* **2010**, *49*, 8593–8597. [CrossRef]
61. Roeffaers, M.B.J.; Sels, B.F.; Uji-i, H.; Blanpain, B.; L'hoëst, P.; Jacobs, P.A.; De Schryver, F.C.; Hofkens, J.; De Vos, D.E. Space-and Time-resolved visualization of acid catalysis in ZSM-5 crystals by fluorescence microscopy. *Angew. Chem. Int. Ed.* **2007**, *46*, 1706–1709. [CrossRef]
62. Ristanovic, Z.; Hofmann, J.P.; De Cremer, G.; Kubarev, A.V.; Rohnke, M.; Meirer, F.; Hofkens, J.; Roeffaers, M.B.J.; Weckhuysen, B.M. Quantitative 3D fluorescence imaging of single catalytic turnovers reveals spatiotemporal gradients in reactivity of zeolite H-ZSM-5 crystals upon steaming. *J. Am. Chem. Soc.* **2015**, *137*, 6559–6568. [CrossRef]
63. Buurmans, I.L.C.; Ruiz-Martínez, J.; van Leeuwen, S.L.; van der Beek, D.; Bergwerff, J.A.; Knowles, W.V.; Vogt, E.T.C.; Weckhuysen, B.M. Staining of Fluid-Catalytic-Cracking Catalysts: Localising Brønsted Acidity within a Single Catalyst Particle. *Chem.—A Eur. J.* **2012**, *18*, 1094–1101. [CrossRef] [PubMed]
64. Whiting, G.T.; Meirer, F.; Valencia, D.; Mertens, M.M.; Bons, A.J.; Weiss, B.M.; Stevens, P.A.; de Smit, E.; Weckhuysen, B.M. Selective staining of Brønsted acidity in zeolite ZSM-5-based catalyst extrudates using thiophene as a probe. *Phys. Chem. Chem. Phys.* **2014**, *16*, 21531–21542. [CrossRef] [PubMed]
65. Kox, M.H.F.; Mijovilovich, A.; Sättler, J.J.H.B.; Stavitski, E.; Weckhuysen, B.M. The Catalytic Conversion of Thiophenes over Large H-ZSM-5 Crystals: An X-Ray, UV/Vis, and Fluorescence Microspectroscopic Study. *ChemCatChem* **2010**, *2*, 564–571. [CrossRef]
66. Chen, C.; Guan, H.; Zhou, J.; Tang, Q.; Zhang, M.H.; Yu, L.; Wang, H.; Qin, Y.C.; Song, L.J. Visualizing acid site accessibility in hierarchical ZSM-5 zeolites through super-resolution fluorescence imaging. *Appl. Catal. A Gen.* **2025**, *707*, 120498. [CrossRef]
67. Ristanovic, Z.; Kubarev, A.V.; Hofkens, J.; Roeffaers, M.B.J.; Weckhuysen, B.M. Single molecule nanospectroscopy visualizes proton-transfer processes within a zeolite crystal. *J. Am. Chem. Soc.* **2016**, *138*, 13586–13596. [CrossRef]
68. Lakowicz, J.R.; Masters, B.R. Principles of fluorescence spectroscopy. *J. Biomed. Opt.* **2008**, *13*, 029901. [CrossRef]
69. Zhao, B.; Summers, F.A.; Mason, R.P. Photooxidation of Amplex Red to resorufin: Implications of exposing the Amplex Red assay to light. *Free Radic. Biol. Med.* **2012**, *53*, 1080–1087. [CrossRef]
70. Li, D.; Garisto, S.L.; Huang, P.J.J.; Yang, J.; Liu, B.; Liu, J. Fluorescent detection of fluoride by CeO_2 nanozyme oxidation of Amplex red. *Inorg. Chem. Commun.* **2019**, *106*, 38–42. [CrossRef]

71. Dębski, D.; Smulik, R.; Zielonka, J.; Michałowski, B.; Jakubowska, M.; Dębowska, K.; Adamus, J.; Marcinek, A.; Kalyanaraman, B.; Sikora, A. Mechanism of oxidative conversion of Amplex® Red to resorufin: Pulse radiolysis and enzymatic studies. *Free Radic. Biol. Med.* **2016**, *95*, 323–332. [CrossRef] [PubMed]
72. Lefrançois, P.; Vajrala, V.S.R.; Arredondo, I.B.; Goudeau, B.; Doneux, T.; Bouffier, L.; Arbault, S. Direct oxidative pathway from amplex red to resorufin revealed by in situ confocal imaging. *Phys. Chem. Chem. Phys.* **2016**, *18*, 25817–25822. [CrossRef] [PubMed]
73. Lee, H.; Kim, K.; Kang, C.M.; Choo, A.; Han, D.; Kim, J. In situ confocal fluorescence lifetime imaging of nanopore electrode arrays with redox active fluorogenic amplex red. *Anal. Chem.* **2022**, *95*, 1038–1046. [CrossRef]
74. Li, B.; He, Z.; Zhou, H.; Zhang, H.; Cheng, T. Reversible fluorescent probes for chemical and biological redox process. *Chin. Chem. Lett.* **2017**, *28*, 1929–1934. [CrossRef]
75. Shen, H.; Tauzin, L.J.; Baiyasi, R.; Wang, W.X.; Moringo, N.; Shuang, B.; Landes, C.F. Single particle tracking: From theory to biophysical applications. *Chem. Rev.* **2017**, *117*, 7331–7376. [CrossRef] [PubMed]
76. Chen, C.; Shi, H.; Cai, X.; Mao, L.; Chen, Z. Enhanced bifunctional photocatalytic performances for H_2 evolution and HCHO elimination with an S-scheme $CoWO_4/CdIn_2S_4$ heterojunction. *Acta Phys.-Chim. Sin.* **2025**, *41*, 100155. [CrossRef]
77. Zhou, X.; Shi, H.; Cai, X.; Yan, G.; Yin, C.W.; Duan, J.B.; Kang, H.P.; Mao, L. Construction and exploration of an S-scheme $ZnTiO_3/ZnIn_2S_4$ photocatalyst for efficient hydrogen production and formaldehyde degradation. *Sep. Purif. Technol.* **2025**, *378*, 134766. [CrossRef]
78. Rong, A.; Zhao, Q.; Shi, H.; Cai, X.; Zhu, H.W.; Chen, C.X.; Zhou, X.; Yan, G.; Mao, L. Fabrication of $CoTiO_3/MgIn_2S_4$ S–scheme heterojunctions with efficient charge separation to enhance the photocatalytic activities of hydrogen generation and formaldehyde removal. *Sep. Purif. Technol.* **2025**, *356*, 130010. [CrossRef]
79. Zhou, X.; Shi, H.; Rong, A.; Wei, M.J.; Chen, C.X.; Chen, Z. Enhanced photocatalytic properties of H_2 production and tetracycline removal with a $H_5PMo_{10}V_2O_{40}/ZnIn_2S_4$ S-scheme heterojunction. *Appl. Surf. Sci.* **2025**, *694*, 162844. [CrossRef]
80. Chen, C.; Shi, H.; Rong, A.; Wei, M.J.; Zhou, X.; Feng, B.; Wang, W.D. Fabrication of $SiW_9Co_3/CdIn_2S_4$ heterojunction with boosted photocatalytic performance for H_2 generation and Cr (VI) reduction. *Int. J. Hydrogen Energy* **2025**, *130*, 249–261. [CrossRef]
81. Li, J.Q.; Hu, J.Y.; Cheng, J. Water effect on the band edges of anatase TiO_2 surfaces: A theoretical study on charge migration across surface heterojunctions and facet-dependent photoactivity. *Phys. Chem. Chem. Phys.* **2023**, *25*, 29143–29154. [CrossRef]
82. Wang, W.K.; Chen, J.J.; Lou, Z.Z.; Kim, S.; Fujitsuka, M.; Yu, H.Q.; Majima, T. Single-molecule and-particle probing crystal edge/corner as highly efficient photocatalytic sites on a single TiO_2 particle. *Proc. Natl. Acad. Sci. USA* **2019**, *116*, 18827–18833. [CrossRef]
83. Zheng, Z.; Huang, B.; Lu, J.; Qin, X.; Zhang, X.; Dai, Y. Hierarchical TiO_2 microspheres: Synergetic effect of {001} and {101} facets for enhanced photocatalytic activity. *Chem.—A Eur. J.* **2011**, *17*, 15032–15038. [CrossRef] [PubMed]
84. D'Arienzo, M.; Carbajo, J.; Bahamonde, A.; Crippa, M.; Polizzi, S.; Scotti, R.; Wahba, L.; Morazzoni, F. Photogenerated defects in shape-controlled TiO_2 anatase nanocrystals: A probe to evaluate the role of crystal facets in photocatalytic processes. *J. Am. Chem. Soc.* **2011**, *133*, 17652–17661. [CrossRef] [PubMed]
85. Banik, A.; Maekawa, H.; Fajardo, J.; Zutter, B.; Alcorn, F.M.; Kumar, S.; Watanabe, K.; Kudo, A.; Ge, N.H.; Talin, A.A.; et al. Unequal {110} Facets: The Potential Role of Intraparticle Heterogeneity and Facet Termination in Photoelectrochemical Activity of Single $BiVO_4$ Particles. *ACS Nano* **2025**, *19*, 6250–6262. [CrossRef]
86. Zhu, J.; Fan, F.; Chen, R.; An, H.; Feng, Z.; Li, C. Direct imaging of highly anisotropic photogenerated charge separations on different facets of a single $BiVO_4$ photocatalyst. *Angew. Chem.* **2015**, *127*, 9239–9242. [CrossRef]
87. Shen, M.; Ding, T.; Hartman, S.T.; Wang, F.; Krucylak, C.; Wang, Z.; Tan, C.; Yin, B.; Mishra, R.; Lew, M.D.; et al. Nanoscale colocalization of fluorogenic probes reveals the role of oxygen vacancies in the photocatalytic activity of tungsten oxide nanowires. *ACS Catal.* **2020**, *10*, 2088–2099. [CrossRef]
88. Huang, T.X.; Dong, B.; Filbrun, S.L.; Okmi, A.A.; Cheng, X.; Yang, M.; Mansour, N.; Lei, S.; Fang, N. Single-molecule photocatalytic dynamics at individual defects in two-dimensional layered materials. *Sci. Adv.* **2021**, *7*, eabj4452. [CrossRef] [PubMed]
89. Wu, L.W.; Lyu, P.T.; Zhang, R.; Chen, K.; Zuo, L.; Song, D.; Feng, Z.Z.; Nie, Y.T.; Cheng, X.; Huang, T.X.; et al. Nanoscale correlation of single-molecule reactivity and charge carrier dynamics in a two-dimensional layered InSe photocatalyst. *Nat. Catal.* **2026**, *9*, 87–94. [CrossRef]
90. Sambur, J.B.; Chen, T.Y.; Choudhary, E.; Chen, G.; Nissen, E.J.; Thomas, E.M.; Zou, N.; Chen, P. Sub-particle reaction and photocurrent mapping to optimize catalyst-modified photoanodes. *Nature* **2016**, *530*, 77–80. [CrossRef]
91. Sambur, J.B.; Shepherd, D.P.; Hesari, M.; Van Erdewyk, M.; Choudhary, E.; Chen, P. Correlated single-molecule reaction imaging and photocurrent measurements reveal underlying rate processes in photoelectrochemical water splitting. *J. Electrochem. Soc.* **2019**, *166*, H3286–H3293. [CrossRef]
92. Okazaki, M.; Suganami, Y.; Hirayama, N.; Nakata, H.; Oshikiri, T.; Yokoi, T.; Misawa, H.; Maeda, K. Site-selective deposition of a cobalt cocatalyst onto a plasmonic Au/TiO_2 photoanode for improved water oxidation. *ACS Appl. Energy Mater.* **2020**, *3*, 5142–5146. [CrossRef]

93. Hirayama, D.; Kawawaki, T.; Oguchi, S.; Ogano, M.; Kon, N.; Yasuda, T.; Higami, A.; Negishi, Y. Ultrafine rhodium–chromium mixed-oxide cocatalyst with facet-selective loading for excellent photocatalytic water splitting. *J. Am. Chem. Soc.* **2024**, *146*, 26808–26818. [CrossRef]
94. Liu, Y.; Shang, J.; Zhu, T. Gas-solid photoelectrocatalytic CO_2 reduction using solid planar photoelectrocatalytic device ITO/RGO/ITO. *Appl. Surf. Sci.* **2023**, *639*, 158196. [CrossRef]
95. Karim, K.M.R.; Tarek, M.; Sarkar, S.M.; Mouras, R.; Ong, H.R.; Abdullah, H.; Cheng, C.K.; Khan, M.M.R. Photoelectrocatalytic reduction of CO_2 to methanol over $CuFe_2O_4$@ PANI photocathode. *Int. J. Hydrogen Energy* **2021**, *46*, 24709–24720. [CrossRef]
96. Zhang, X.; Ji, X.; An, W.; Wang, H.; Guo, H.X.; Cui, W.Q. Regulating of d-band center of Cu catalysts for enhanced photoelectrocatalytic reduction of CO_2. *Appl. Surf. Sci.* **2025**, *716*, 164619. [CrossRef]
97. Turksoy, A.; Yildiz, D.; Akkaya, E.U. Photosensitization and controlled photosensitization with BODIPY dyes. *Coord. Chem. Rev.* **2019**, *379*, 47–64. [CrossRef]
98. Johnson, T.W.; Lapin, Z.J.; Beams, R.; Lindquist, N.C.; Rodrigo, S.G.; Novotny, L.; Oh, S.H. Highly reproducible near-field optical imaging with sub-20-nm resolution based on template-stripped gold pyramids. *ACS Nano* **2012**, *6*, 9168–9174. [CrossRef]
99. Borhan, A.I.; Ghemes, A.I.; Husanu, M.A.; Popescu, D.G.; Borca, C.N.; Huthwelker, T.; Radu, I.; Dirtu, A.C.; Dirtu, D.; Bulai, G.; et al. Carbon-based heterostructure from multi-photo-active nanobuilding blocks $SrTiO_3$@ $NiFe_2O_4$@Fe^0@Ni^0@ CNTs with derived nanoreaction metallic clusters for enhanced solar light-driven photodegradation of harmful antibiotics. *Appl. Surf. Sci.* **2023**, *622*, 156987. [CrossRef]
100. Trung, V.Q.; Phu, N.D.; Van Hai, P.; Dong, C.L.; Nga, T.T.T.; Chou, W.C.; Hue, N.T.N.; Hue, P.T.; Tuyen, L.A.; Hung, N.Q.; et al. Enhancing photocatalytic performance in Bi_2WO_6 nanolayers via ultrasound-assisted oxygen vacancy engineering. *J. Alloys Compd.* **2025**, *1010*, 177747. [CrossRef]
101. Fei, Y.; Fu, S.; Shi, W.; Fang, K.; Wang, R.; Zhang, T.; Li, Y. Scalable and lightweight deep learning for efficient high accuracy single-molecule localization microscopy. *Nat. Commun.* **2025**, *16*, 7217. [CrossRef]

Disclaimer/Publisher's Note: The statements, opinions and data contained in all publications are solely those of the individual author(s) and contributor(s) and not of MDPI and/or the editor(s). MDPI and/or the editor(s) disclaim responsibility for any injury to people or property resulting from any ideas, methods, instructions or products referred to in the content.